CORONAVIRUS

Nanobody assemblies with fully flexible topology enabled by genetically encoded tetrazine amino acids

Elise M. Van Fossen¹, Riley M. Bednar¹, Subhashis Jana¹, Rachel Franklin¹, Joseph Beckman^{1,2}, P. Andrew Karplus¹, Ryan A. Mehl¹*

Assembling nanobodies (Nbs) into polyvalent multimers is a powerful strategy for improving the effectiveness of Nb-based therapeutics and biotechnological tools. However, generally effective approaches to Nb assembly are currently restricted to the amino or carboxyl termini, greatly limiting the diversity of Nb multimer topologies that can be produced. Here, we show that reactive tetrazine groups—site-specifically inserted by genetic code expansion at Nb surface sites—are compatible with Nb folding and function, enabling Nb assembly at any desired point. Using two anti-SARS-CoV-2 Nbs with viral neutralization ability, we created Nb homo- and heterodimers with improved properties compared with conventionally linked Nb homodimers, which, in the case of our tetrazineconjugated trimer, translated into enhanced viral neutralization. Thus, this tetrazine-based approach is a generally applicable strategy that greatly increases the accessible range of Nb assembly topologies, and thereby adds the optimization of topology as an effective avenue to generate Nb assemblies with improved efficacy.

Copyright © 2022 The Authors, some rights reserved; exclusive licensee American Association for the Advancement of Science. No claim to original U.S. Government Works, Distributed under a Creative Commons Attribution NonCommercial License 4.0 (CC BY-NC).

INTRODUCTION

Single-domain antibodies, commonly referred to as nanobodies (Nbs; Fig. 1A), are small (~15 kDa) protein binders derived from Camelidae antibodies. Nbs are stable, easy-to-produce, highly modifiable alternatives to conventional antibodies and are often used as therapeutic, diagnostic, imaging agents and tools for structural biology studies (1). The generation of multivalent Nb assemblies from Nb monomers has proven to be a powerful strategy for generating Nb-based therapeutics, as these assemblies have high avidity that enhances binding (2) as well as longer lifetimes (3) and the ability to bind multiple, diverse targets (4). More recently, the multimerization of Nbs targeted against severe acute respiratory syndrome coronavirus 2 (SARS-CoV-2) has been shown to enhance their abilities both as binders and as therapeutics against viruses, and their small size opens access to self-administration through nebulizers or nasal spray (5, 6). As the demand for Nb multimerization and functionalization increases, so will the need for conjugation strategies that access the full possible range of assembly geometries, allowing avidity to be optimized for each targeted application without interfering with Nb binding.

Nb binding potential stems from three complementaritydetermining regions (CDRs) supported by conserved β sheet–based domain framework. While all three CDR loops contribute to binding, the CDR3 loop has the highest variability with respect to loop length and position, as it can protrude outward from the N terminus or fold over onto the side of the domain when participating in target binding (Fig. 1A) (7). Because of the variability of the CDR loops, care must be taken to functionalize and multimerize Nbs in a manner that will not impede their target binding (8).

Nb assembly is typically accomplished by genetic fusions, either linking Nbs in tandem, or linking them to multimerization domains (Fig. 1B). These strategies restrict the Nb conjugation sites to the N or C termini, which, because of their close proximity to CDR regions, can be deleterious for binding interactions. Genetic fusions

also limit the linker distances between multimeric Nbs and can compromise multimer stability (9). Covalent and noncovalent Nb multimerization has been achieved via connections to multimeric scaffolding protein itself limits the orientation and distance between terminal Nbs (10–12).

As the field transitions to developing therapeutic protein-protein conjugates that replace genetic fusions with flexible organic polymer linkers, it is advantageous to develop modular, site-specific connections for efficient assembly of protein architectures. Site-specific functionalization with noncanonical amino acids (ncAA) using genetic code expansion (GCE) provides freedom of attachment and has been used successfully to link molecules intended for therapeutic usage, including drug-antibody conjugates, PEGylated proteins, and usage, including drug-antibody conjugates, PEGylated proteins, and conjugative protein dimerization for bispecific antibody formation (13–15). Unfortunately, these ligation reactions can require multiple conjugation steps, toxic catalysts, nonphysiological pHs or long incubation times (on the order of days), and high label concentrations to achieve sufficient protein coupling yields (16).

While GCE-produced Nb conjugates have advanced cell targeting and imaging with small molecules (17), peptides (18), and quantum dots (19), GCE has yet to be used in generating Nb assemblies or Nb-protein conjugates, suggesting an incompatibility of available conjugation approaches with these systems (20). The value of flexible linkers and minimal scaffolding has been demonstrated by the improved affinity of polyethylene glycol (PEG)-linked dimeric and tetrameric Nb assemblies using a sortase tagging method combined with strain-promoted azide alkyne cycloaddition. Unfortunately, this approach allows very limited Nb assembly topologies (forced by C-terminal linkages and the required long 2- to 4-day coupling reactions during which protein quality can degrade). As such, the production of chemically pure conjugated Nb assemblies intended for therapeutic use stands to benefit from approaches that (i) grant freedom of attachment and (ii) use high-yielding, efficacious, and specific labeling reactions that occur under biologically compatible time frames and conditions.

Recently, our laboratory has developed a number of GCE systems for incorporating tetrazine-containing ncAAs that undergo ultrafast

¹Department of Biochemistry and Biophysics, Oregon State University, Corvallis, OR 97331, USA. ²e-MSion, Inc., 2121 NE Jack London Drive, Corvallis, OR 97330, USA. *Corresponding author. Email: ryan.mehl@oregonstate.edu

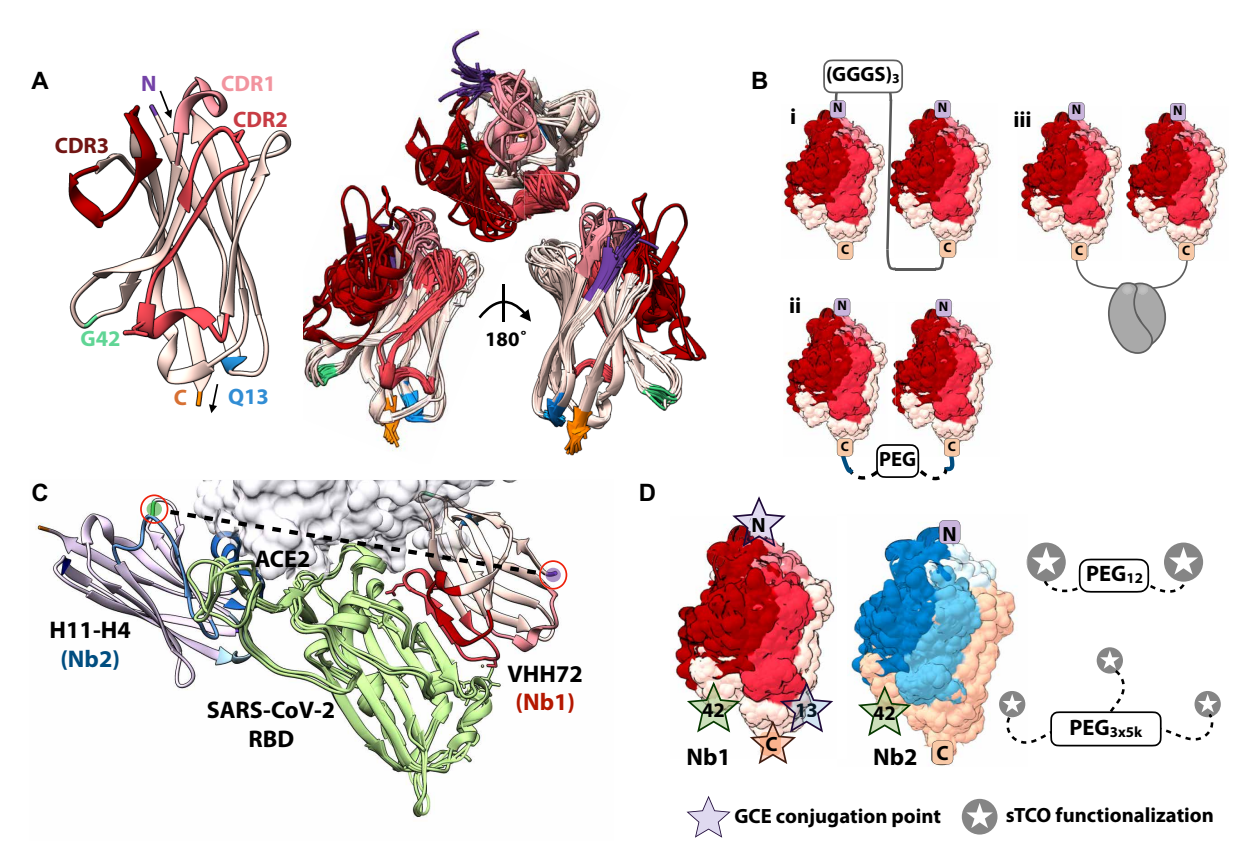


Fig. 1. Structural features of Nbs and potential assembly strategies. (A) Ribbon diagram of Nb1 (VHH72, PDB_ID 6WAQ) as a representative Nb, highlighting three complementarity-determining regions (CDRs) (shades of red), the N terminus (purple), the C terminus (orange), and framework sites Q13 (cyan) and G42 (green). Shown to the right are front, back, and top views of 30 overlaid Nb structures from the Protein Data Bank (PDB) (7) (with the same coloring). (B) Three common Nb dimerization modes are shown using a generic cartoon Nb domain [CDRs colored as in (A)]: (i) tail-to-head genetic conjugation, (ii) dimerization domain-mediated, and (iii) sortase A-mediated. (C) Ribbon diagrams showing distinct severe acute respiratory syndrome coronavirus 2 (SARS-CoV-2) receptor binding domain (RBD) (pale green) epitopes recognized by Nb1 (red tone CDRs; PDB_ID 6ZH9) and Nb2 (blue tone CDRs; PDB_ID 6WAQ). ACE2 (semitransparent gray surface) is also shown as it binds to the SARS-CoV-2 RBD (PDB_ID 6MOJ). A dashed line connects the Nb1 N terminus (purple) and Nb2 residue 42 (green) positions that we will use to link the Nbs. (D) Nb and PEG-linker components used in this study, with various positions of Tet3.0 incorporation for Nb1 (red CDRs) and Nb2 (blue CDRs) indicated by stars [colored as in (A)], and sTCO-functionalized groups on the PEG linkers indicated by circled stars. Images and overlays are generated by Chimera (38). GCE, genetic code expansion.

reactions ($k_2 \sim 8 \times 10^4 \text{ M}^{-1} \text{ s}^{-1}$) with strained *trans*-cyclooctenes, allowing us to achieve substoichiometric labeling of tetrazine-containing proteins, within living cells and on surfaces (21-24). We hypothesized that this GCE-encoded, tetrazine bioorthogonal reaction combined with flexible polymer linkers, which, for convenience, we refer to it here as "Tet-link" technology, could lead to more complex Nb assemblies with increased functionality by allowing precision conjugations to be performed at previously underutilized surface residues to assemble scaffolds that maximize target binding.

Here, we explore this possibility by seeking to generate improved multimeric Nb assemblies as potential anti–SARS-CoV-2 therapeutic agents that target the receptor binding domain (RBD) of the SARS-CoV-2 spike protein. By site-specifically encoding a reactive tetrazine ncAA at multiple positions along the framework of existing anti-RBD Nbs, we demonstrate that this fast and gentle GCE-encoded tetrazine coupling reaction allows the generation of fully functional anti–SARS-CoV-2 homodimeric Nbs with unique assembly geometries, allowing the identification of conjugation locations that exhibit improved binding compared with a genetic fusion. We further show the versatility of the approach by generating an Nb heterodimer that can target independent RBD epitopes and an Nb homotrimer,

designed to target the trimeric organization of the spike protein that exhibits enhanced neutralization abilities (4, 25).

RESULTS

Strategy

To assess the power of Tet-link technology as a platform for a versatile combinatorial approach to making defined high-affinity Nb assemblies in virtually any system, we selected two Nbs that can neutralize SARS-CoV-2 by recognizing distinct epitopes on the RBDs of the SARS-CoV-2 spike protein (Fig. 1C).

For our initial assessment on the effects of varying the point of attachment for Nb dimers, we chose the "VHH72" Nb, which we refer to as Nb1. This variant was one of the first examples of an Nb that was identified to bind the SARS-CoV-2 RBD (26). Although originally selected to bind SARS-CoV-1 RBD, Nb1 exhibited modest binding against SARS-CoV-2 RBD, and tail-to-head genetic dimerization improved its binding and neutralization abilities (26).

The forms of Nb1 we created for this study include tail-to-head genetically linked dimer and trimer versions. These serve as benchmarks with which to compare GCE-conjugated multimers against genetically conjugated multimers. For the generation of Tet-linked Nb assemblies, Nb1 monomers were designed with the Tet3.0 ncAA installed at one of four distinct GCE-enabled linkage points, including, at the N and C termini (referred to as Nb1_N and Nb1_C, respectively) and at the framework positions Gln13 (Nb1₁₃) and Gly42 (Nb1₄₂), two Nb framework sites that are structurally distinct (Fig. 1D) (*27*). These four linkage points are a subset of a group of five sites that have been previously shown to be amenable to ncAA incorporation without compromising Nb stability or binding (*19*) and additionally are predicted to not interfere with the binding region specifically of Nb1 (Fig. 1A) as Nb1 interactions with SARS-CoV-2 RBD chiefly occur along the side of the Nb, extending down almost its entire length (Fig. 1C).

The second Nb, which we refer to as Nb2, is the "H11-H4" Nb (28). This Nb recognizes a distinct RBD epitope compared with Nb1 (Fig. 1C) and thus can be used for making biparatopic heterodimers. Nb2 boasts a low nanomolar dissociation constant (K_d) (5 nM) as a monomer and exhibits potent neutralization ability as an Fc-mediated dimer [neutralization doses (ND50) of ~4 to 6 nM] (Fig. 1B). For the linkage chemistry, we used a tetrazine-derivatized phenylalanine ncAA (Tet3.0) previously developed by our laboratory, which is compatible with Escherichia coli and mammalian GCE systems (21) that covalently react with conformationally strained trans-cyclooctene (sTCO) head

groups. It has been well documented that the size, flexibility, and composition of Nb multimerizing scaffolds significantly affect the function of the final anti–SARS-CoV-2 Nb multimers (29), and so, for the linker itself, we selected PEG linkers that grant the scaffold increased flexibility and have literature precedent for high biocompatibility (29). For the dimers, the length of the linker (PEG₁₂) was chosen to be similar to the length of the previously published genetic dimer (12 amino acids) to allow direct comparisons to be made between genetically and GCE-conjugated dimers. For the trimeric Nb multimer, our goal was to allow the conjugated Nbs full access to the trimeric target regardless of orientation; therefore, we selected a three-headed (PEG) $_{3x5k}$ linker because of its abundant length (Fig. 1D).

Producing ligation-capable Nb building blocks

Most constructs were designed with cleavable N-terminal His- and bdSUMO-tags to facilitate expression and purification (Fig. 2A). This included the control "tail-to-head" genetically linked dimer (Nb1-Nb1) and trimer (Nb1-Nb1) that have (GGGS)₃ linkers as described by Wrapp et al. (26). One exception was the Nb1 construct encoding Tet3.0 at the C terminus for which truncation products not containing Tet3.0 would be nearly identical in length and therefore difficult to purify away from the desired full-length product. To avoid this potential problem, we appended a tobacco etch virus

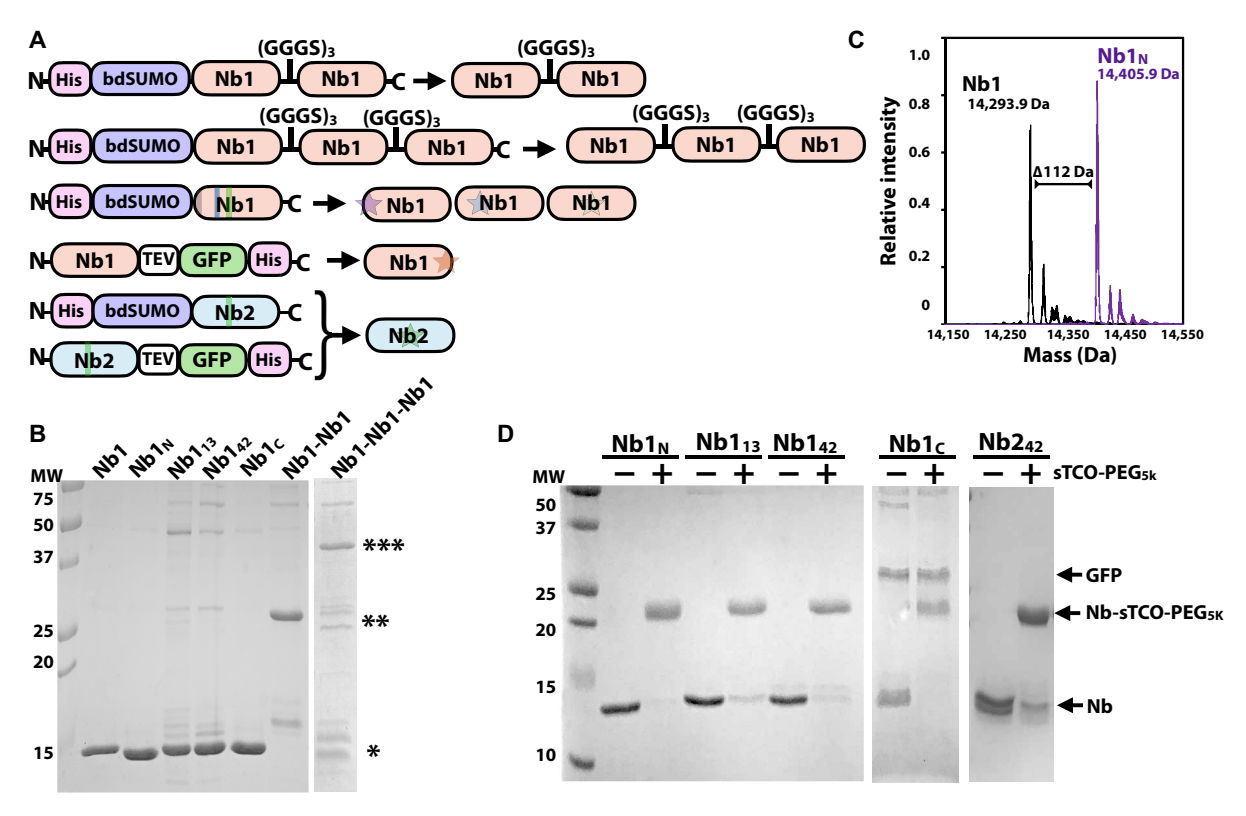


Fig. 2. Expression of Tet3.0-encoded Nbs and validation of Tet3.0 reactivity. (A) Constructs used for Nb1 and Nb2 expressions are shown in the boxes and the mature protein products derived from each are on the right after the arrows. Indicated are the sites of amber codons for each construct (colored stripes) and the positions of Tet3.0 in the mature proteins (colored stars) (colored as in Fig. 1A). (B) Fifteen percent SDS-polyacrylamide gel electrophoresis (PAGE) molecular weight standards and purified Nb monomers (migrating at ~15 kDa, indicated by a single asterisk, Nb1-Nb1 genetic homodimer is indicated by a double asterisk, and Nb1-Nb1-Nb1 genetic trimer is indicated by a triple asterisk) with labels above each lane. (C) Electrospray ionization mass spectrometry analyses of Nb1 monomer (black trace) and Nb1_N (purple trace). Observed (black arrows) and expected masses are listed and the change in side chain at the N-terminal position (Gln versus Tet3.0) is shown with the expected mass shift. (D) SDS-PAGE gel showing molecular weight standards and the mobility of each Tet3.0-containing Nb in the absence ("-") and presence ("+") of sTCO with PEG_{5k} as noted above each lane. GFP, green fluorescent protein; TEV, tobacco etch virus.

(TEV)–cleavable green fluorescent protein (GFP) domain and His tag to the C terminus of the construct. We also used this C-terminal extension for the Nb2 construct to be used in the assembly of an Nb1-Nb2 heterodimer, so that the additional mass of the GFP and its fluorescence would assist in isolation of the desired heterodimer from potentially contaminating homodimer products.

Expression and purification, including cleavage of the solubility tags, for all targeted Nb1 and Nb2 forms resulted in reasonable yields of Tet3.0-encoded Nb, ranging from 5 to 30 mg/liter of culture (Fig. 2B and table S1). The incorporation of intact Tet3.0 was confirmed using Nb1_N as a representative example, with electrospray ionization mass spectrometry (MS), with a mass shift of +112 Da observed in Nb1N compared to WT, which agrees well with the expected +113-Da difference between Tet3.0 and the native Gln (Fig. 2C). The precise location of the Tet3.0 was additionally confirmed with MS confirming the site specificity of our technique (fig. S5). The reactivity of each Tet3.0-Nb was then confirmed by incubation with an sTCO-PEG5k polymer for 10 min on ice. In each case, more than 95% of the protein sample exhibited a mobility shift as determined by SDS-polyacrylamide gel electrophoresis (PAGE), indicating excellent reactivity of the incorporated Tet3.0 (Fig. 2D).

The site of homodimerization of Nb1 affects binding ability

With Tet-link technology, we next generated homodimers of each Nb1 form—Nb1_N, Nb1₁₃, Nb1₄₂, and Nb1_C—to be evaluated alongside the Nb1-Nb1 control (Fig. 3A). As our objective at this stage was simply to produce sufficient quantities of material for testing, a simple one-pot reaction was attempted and determined to be adequate for our purposes (see Materials and Methods). Each Tet3.0-Nb1 variant was reacted with a two-headed sTCO (PEG)₁₂ linker (Fig. 1D), during a brief 10-min incubation on ice yielding a 40 to 80% homodimer product that was purified away from any unreacted material via size exclusion chromatography (SEC) (Fig. 3B and fig. S6). With biolayer interferometry (BLI), we evaluated the affinity of each homodimer toward immobilized SARS-CoV-2 RBD, and in each case, the data fit well to a single binding event (Fig. 3C and Table 1). The control Nb1-Nb1 genetic tail-to-head dimer yielded a K_d of ~89 nM, providing a reference value to which all other variants could be compared (Fig. 3D). (Nb1₄₂)₂, (Nb1₁₃)₂, and (Nb1_N)₂ dimers bound 3- to 7-fold tighter and (Nb1_C)₂ bound ~1.5-fold weaker. The higher affinities of (Nb1₄₂)₂ and (Nb1_N)₂ were observed to be due to both a higher association rate and a concomitant slower dissociation rate, whereas the (Nb1₁₃)₂ improvement was due solely to a distinctively slower disassociation rate (Table 1).

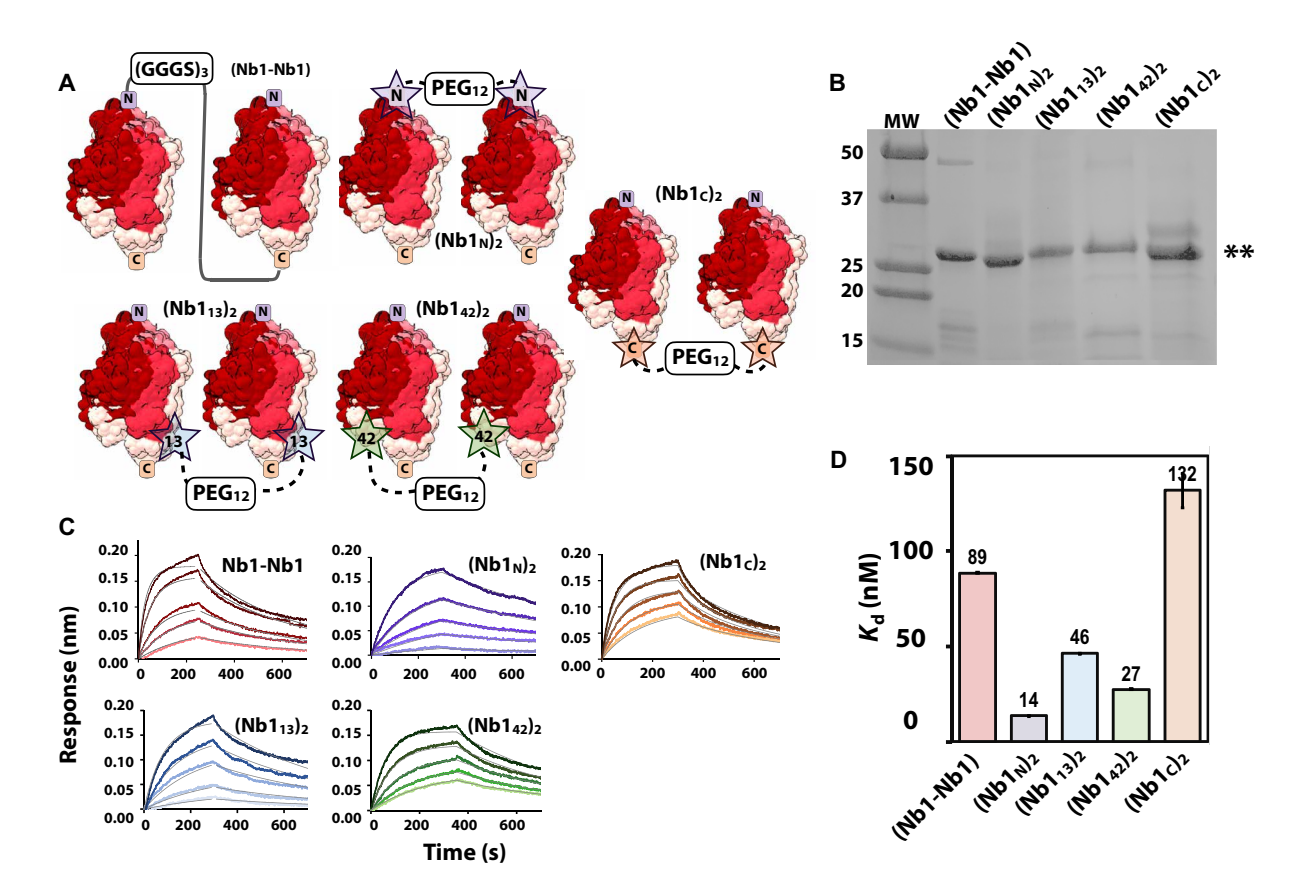


Fig. 3. Evaluation of the effect of point of conjugation on SARS-CoV-2 RBD interaction by Nb1 dimers. (A) Homodimeric conjugations of Nb1 generated in this study, with points of conjugation indicated by stars. (B) Four to 20% gradient SDS-PAGE gel of purified Nb homodimers as labeled above each lane. "**" indicates expected migration of homodimers at ~30-kDa Nb. (C) Sensorgrams for biolayer interferometry (BLI) analysis of conjugated Nbs with immobilized SARS-CoV-2 RBD. Concentrations on conjugated Nbs ranged from 2 to 1500 nM for each assay (table S2), and global fits were obtained by fitting the sensorgrams to a 1:2 binding curve (light gray line). Only fits with an R^2 value greater than 0.97 were considered acceptable. (D) K_d values plotted for all conjugated Nbs; the Nb corresponding to the K_d is indicated under the plot.

Construct	$k_{\rm on} (1/{\rm Ms}) \times 10^4$	$k_{\rm off} (1/s) \times 10^{-3}$	K_{d} (nM)
Nb1-Nb1	3.54 ± 0.04	3.14 ± 0.03	89 ± 1
(Nb1 _N) ₂	8.58 ± 0.04	1.186 ± 0.006	13.8 ± 0.1
(Nb1 ₁₃) ₂	3.38 ± 0.07	1.56 ± 0.03	46 ± 1
(Nb1 ₄₂) ₂	7.31 ± 0.04	2.01 ± 0.01	27.5 ± 0.2
(Nb1 _C) ₂	4.81 ± 0.01	6.4 ± 0.4	132±8
(Nb1 _N)-(Nb2 ₄₂)	15.07 ± 0.08	0.593 ± 0.003	3.93 ± 0.03
Nb1-Nb1-Nb1	5.79 ± 0.08	1.56 ± 0.04	27.9 ± 0.8
(Nb1 _N) ₃	24.6 ± 0.2	0.566 ± 0.004	2.31 ± 0.02

Heterodimeric and trimeric Nbs with potential as enhanced SARS-CoV-2 therapeutics

Of great interest was to demonstrate that our technology could also be used to make a heterodimeric Nb assembly targeting two separate epitopes on the RBD, which should enhance viral neutralization and hinder the development of viral resistance (4). To synthesize a GCE-enabled biparatopic Nb dimer, we selected Nb1_N (as the tightest binder among the Nb1 constructs) and coupled it with Nb2 (introduced above; Fig. 1C). For Nb2, we selected Gly42 as a linkage site that should not interfere with its RBD interactions and that is on the side of Nb2 expected to be closest to Nb1 when both are bound to a single RBD (Figs. 1C and 4A). To resolve the heterodimeric product from a potential mixture of reaction products, we appended a cleavable GFP tag to Nb2, adding both bulk and a fluorescent signature to the Nb1_N-Nb2₄₂ heterodimer compared to the (Nb1_N)₂ homodimer (fig. S7). The uncleaved Nb242-TEV-GFP protein (Fig. 2A) and an excess of Nb1_N were reacted with a two-headed sTCO (PEG)₁₂ linker (Fig. 1D) in a one-pot manner and the heterodimeric product was purified from reaction products via SEC (Fig. 4A and fig. S7). This Nb1_N-Nb2₄₂ heterodimer was analyzed by BLI and found to have a K_d of ~4 nM for 1:1 binding of the RBD (Fig. 4A and Table 1), closely matching the observed K_d of the Nb2 monomer [~5 nM (28)].

To highlight the potential of the Tet-link strategy to make Nb assemblies matching specific aspects of target topologies, we chose to assemble an Nb1 trimer as this would congruently match the stoichiometry of the trimeric SARS-CoV-2 spike protein (Fig. 4, B and E). Using Nb1_N, the tightest binding of the Nb1 constructs, we generated such a trimer by conjugating it with a three-armed tri-sTCO PEG_{3x5k} linker (Fig. 1D) in a simple, one-pot reaction, with excess Tet3.0-Nb1_N to ensure full loading of each tri-sTCO linker (fig. S8). The fully loaded Nb trimer, (Nb1_N)₃, was separated from other products and MS revealed it to be a single population with a mass of ~58 kDa (fig. S8). This Tet-link approach yielded plenty of material for BLI analysis, mass spectrometric analysis, and neutralization assays, in contrast to the poor expression of a genetic trimer (Nb1-Nb1-Nb1), which only granted sufficient material for BLI assays (table S1). By BLI, $(Nb1_N)_3$ exhibited a K_d of ~2 nM for the SARS-CoV-2 RBD (Fig. 4C and Table 1), roughly 44-fold tighter than the Nb1-Nb1 genetic dimer and 12-fold tighter than the Nb1-Nb1-Nb1 genetic trimer (Fig. 4D). The 12-fold tighter binding compared to the genetic trimer can be attributed to a ~4-fold higher k_{on} and a 3-fold lower k_{off} (Fig. 4, C and D, and Table 1).

GCE-enabled Nb assemblies neutralize SARS-CoV-2 pseudotyped viruses

It is important to note that, for our previous BLI assay results, we used an immobilized, monomeric form of the RBD, such that the true effects of Nb trimerization against a trimeric S protein target may differ from what is seen in these experiments (Fig. 4E). To directly test the extent to which the improved binding of (Nb_N)₃ seen in the BLI experiments translates into an increased SARS-CoV-2 neutralization ability, we compared (Nb_N)₃ with (Nb_N)₂ and Nb1-Nb1 in a standard luciferase-based pseudovirus neutralization assay with HIV-derived lentiviral particles containing the S protein of SARS-CoV-2 (30, 31). In addition, we evaluated the neutralization ability for the same set of Nbs on pseudovirus lacking SARS-CoV-2 spike protein that should maintain infectivity regardless of Nb preincubation [vesicular stomatitis virus G protein (VSV-G) control; fig. S9B]. Among the three Nb assemblies tested, the (Nb_N)₃ trimer was the only one to exhibit significant neutralization ability over the VSV-G control and achieved 96% neutralization at the highest concentration tested (Fig. 4F). Between the two dimers, (Nb_N)₂ and Nb1-Nb1, there was no significant difference in neutralization efficacy.

DISCUSSION

Engineered proteins have transformed the therapeutic landscape, providing powerful approaches to treat diseases with improved efficacy (32), as seen by the success of many drug-antibody conjugates, bispecific antibodies, and imaging agents (16, 33). As the field of engineered protein therapeutics expands to developing therapeutic Nb conjugates tailored to targets with unique and dynamic topologies, it is essential to develop efficient and modular approaches to connect Nbs in a topology that enhances their ability and utility as therapeutics.

Using two previously characterized Nbs against distinct epitopes on the SARS-CoV-2 spike protein RBD as practical examples, we have shown that Tet-link technology provides a flexible, facile, and generally applicable approach for generating diverse Nb assemblies with unique conjugation points. We found that every conjugation point we tested (selected because previous literature suggests that Nb conjugation at those sites would minimally effect Nb binding) incorporated Tet3.0 with good yield, showcasing the amenability of Nbs to GCE incorporation.

We evaluated $(Nb1_N)_2$, $(Nb1_C)_2$ termini-linked homodimer conjugations along with $(Nb1_{13})_2$, $(Nb1_{42})_2$ framework-linked homodimer conjugations in direct comparison to an Nb1-Nb1 genetic conjugation. We observed that three of the four homodimers displayed improved affinity compared to the genetic tail-to-head linkage, showcasing the viability of our approach, and revealing that the site of attachment is a crucial design parameter that grants access to Nb assemblies with improved properties. The unexpected finding that the $(Nb1_N)_2$ conjugation led to the tightest binding despite the close proximity of the N terminus to the CDR regions highlights the general need for screening multiple conjugation options. We speculate that this was possible because the binding interface, composed of both CDR2 and CDR3 loops, extends down the side of the Nb instead of being centered at its top.

The high efficiency of tetrazine-mediated conjugations opens the door for a wide variety of Nb assembly options, as we have illustrated here through the generation of heterodimers and homotrimers. These assemblies are especially advantageous for the development of SARS-CoV-2 therapeutics in distinct ways, as the heterodimer has

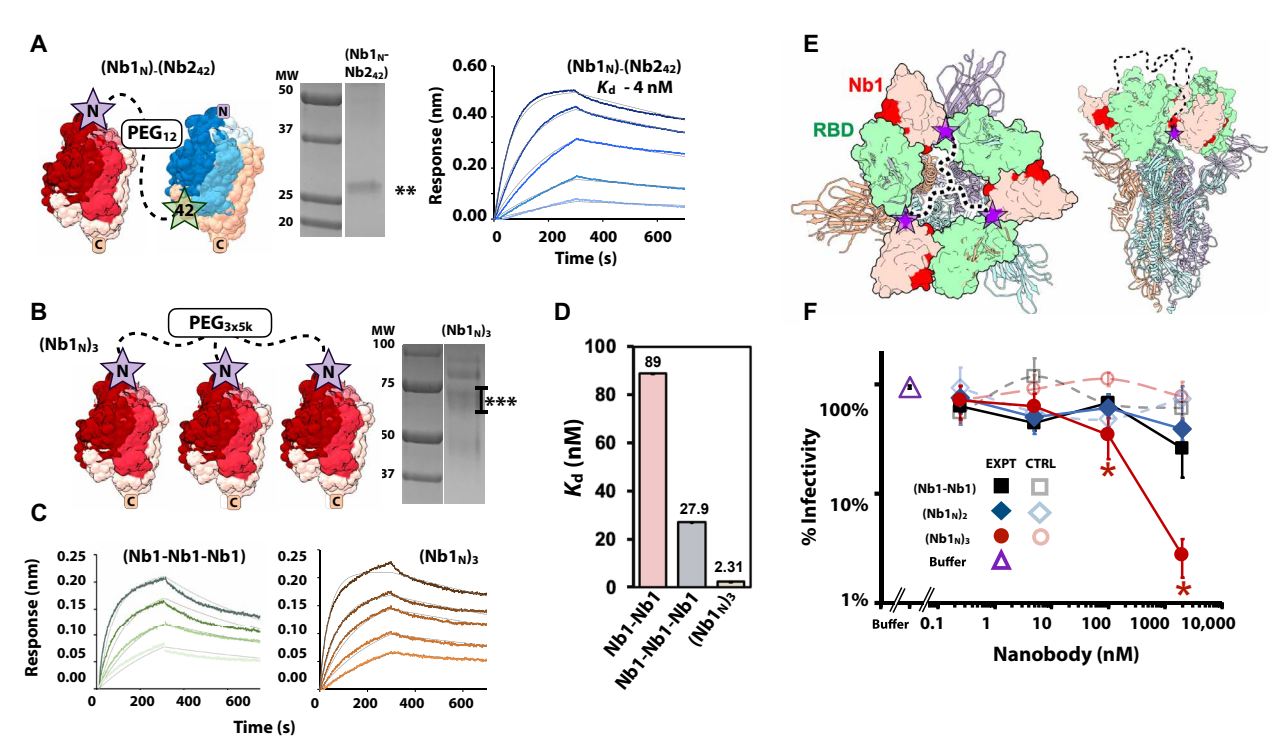


Fig. 4. Generation and evaluation of GCE-conjugated Nb multimers. (**A**) Left: Heterodimeric conjugation of Nb1-Nb2 noting conjugation points (stars). Middle: SDS-PAGE gel of purified Nb1-Nb2. "**" indicates expected heterodimer migration. Right: BLI sensorgrams for heterodimer binding with immobilized RBD showing 1:1 stoichiometry fits (gray lines). (**B**) Left: Trimeric conjugation of (Nb1_N)₃ noting conjugation points (stars). Right: SDS-PAGE gel of purified (Nb1_N)₃, "***" indicates expected trimer migration, which runs as a broad band owing to the PEG_{3x5k} linker. (**C**) BLI sensorgrams of genetic and Tet-linked trimers with immobilized RBD showing 1:2 and 1:1 stoichiometry fits, respectively (gray lines). (**D**) Comparison of K_d values for Nb1-Nb1, Nb1-Nb1-Nb1, and (Nb1_N)₃. (**E**) Three Nb1:RBD complexes (space-filling pink Nb1 with red CDRs and teal RBD; PDB entry 6waq) arranged as a PEG-linked trimer (purple stars and black dotted lines) with the RBDs aligned onto a spike trimer (colored ribbons; PDB entry 7ksg) prepared with Chimera MatchMaker (38). (**F**) Log/log plot of SARS-CoV-2 neutralization assay. Active pseudovirus (with spike protein) pretreated with Nb conjugates [bold filled symbols as indicated in the experimental (EXPT) column] or buffer (purple triangle) are compared to a VSV-G pseudovirus (without spike protein) incubated with Nb conjugates [pale open symbols as indicated in the control (CTRL) column]. EXPT values that are significantly different (P < 0.05) from the corresponding CTRL values are indicated with red asterisks. The analysis of variance (ANOVA) single-factor P values for the two observations with P < 0.05 were P = 0.020 and P = 0.006 for the 100 and 2000 nM data points, respectively.

the potential to target independent sites on the RBDs and thereby limit viral escape (Fig. 4A) and the homotrimer precisely targets the trimeric organization of the spike protein (Fig. 4E) (4, 25). We found that the $K_{\rm d}$ of the heterodimeric conjugation was ~4, which is very similar to the reported $K_{\rm d}$ of the Nb2 monomer (~5 nM), indicating that the conjugation of Nb1 to Nb2 did not negatively affect binding of the monomeric Nb2, nor did it enhance it. In addition, the observed binding fits best to a 1:1 binding model, which implies that a single Nb (Nb2) dominated the interaction. Both observations align with the fact that the $K_{\rm d}$ for the Nb2 monomer is at least 10 times tighter than the Nb1 monomer.

Our homotrimeric Nb assembly, made with the same N-terminal linkage site that generated the best-performing Tet-linked homodimer, enhanced the binding 44-fold over the genetically linked homodimer (Nb1-Nb1) and 12-fold over the genetically linked Nb trimer (Nb1-Nb1-Nb1) controls. Furthermore, it was observed that, with each addition of a genetically linked Nb domain (monomer to dimer to trimer), the expression yields dropped markedly. Notably, this limitation is side-stepped by using the Tet-link technology in a one-pot conjugation of the individual Tet3.0-encoded monomers into a trimer. The higher yields of the Tet-linked trimer allowed sufficient material for SARS-CoV-2 pseudovirus neutralization assays, in comparison to the low yields of the genetic trimer. The

results of the SARS-CoV-2 pseudovirus neutralization assays showed that the binding enhancement observed in the trimeric assembly translated into increased neutralization ability when compared to both the genetically conjugated and GCE-conjugated dimers. Similarly, a recent study using designed RBD mini-binders also showed that SARS-CoV-2 neutralization was improved by trimerization, and that the topology of trimerization mattered, although, in that case, the topologies tested were all limited to genetic linkages through the N and C termini (34).

This Tet-link technology provides both optimal chemistry and unfettered attachment points to functionalize Nbs with no restrictions from bioorthogonal conjugation conditions. Furthermore, the recent optimization of Tet3.0 GCE technology in mammalian cells (21) and the simple two-step, 80% yield chemical synthesis of Tet3.0 ncAA (21) allow for the production of Tet3.0-Nb therapeutics from conventional mammalian sources. Thus, this conjugation approach allows researchers to access the full combinatorial diversity of homoand hetero-Nb assemblies with facile screening of many possible sites of conjugation (each representing a different topology), as well as linkers of varying length and geometry. While the Tet-link sites in this work were informed by generic Nb binding, we expect site selection that is optimized for the specific Nbs, and their target would grant higher avidity. Tet-link offers the ability to quickly

screen both "generic" and "tailored" framework sites as well as linker length and composition for improved avidity (4). This becomes more critical, as Nb assemblies are designed to target complex protein assemblies as well as rapidly mutating protein targets. This rapid assembly and screening of combinatorically fused Nb architectures will be advantageous to therapeutic Nb development (35) when optimizing for pharmacological properties (therapeutic window, lifetime, toxicity, etc.) and will especially provide an advantage when combating rapidly evolving viral targets, such as SARS-CoV-2.

MATERIALS AND METHODS

Molecular cloning

Molecular cloning of plasmids used in this study (table S3) was constructed in the following manner. Previously published Nb sequences [VHH72 (26) and H11-H4 (28)], containing at least 25 base pairs of homology at their flanking ends to either the vector backbone or other fragments, were optimized for expression in *E. coli* and synthesized by Integrated DNA Technologies (Coralville, IA) (table S4). The VHH72 dimer was constructed by differentially codon-optimizing two VHH72 monomers, linked by a glycine-serine linker (GGGGS₃) so that, though the amino acid sequence for the two monomers was identical, the nucleic acid sequences differed enough in such a way that, if desired, TAG sites could be preferentially added to each monomer. Plasmids were then assembled as described in the "Plasmid assembly" section in the Supplementary Materials.

Protein expression

Approximately 50 ng of each plasmid was combined with BL21(ai) E. coli cells or, in the case of Nb1-Nb1-Nb1, Origami B(DE3) Competent Cells. For the expression of Tet-Nbs, each TAG site containing expression plasmid was cotransformed with a GCE machinery plasmid using chemical transformations [Table 1, plasmid 1 (21)]. Cultures (5 ml) were inoculated by scraping a swath of cells containing the appropriate plasmids from a fresh LB agar plate and were grown overnight in 2XYT (no more than 16 hours) in the presence of appropriate antibiotics. Overnight cultures were then used to inoculate expression cultures of ZY media (0.1 to 1.0 liter), supplemented with appropriate antibiotics. For the expression of Tet3.0-Nbs, the media were also supplemented with Tet3.0 (at a final concentration of 500 µM, diluted from a freshly prepared 100 mM solution solubilized in N,N'-dimethylformamide). Cultures were grown with constant shaking at 275 rpm in baffled flasks at 37°C, until they reached an OD₆₀₀ (optical density at 600 nm) of 1.5, wherein they were induced with a final concentration of 0.1% arabinose. Upon induction, the temperature was decreased to 18°C (or 30°C in the case of Nb1-Nb1-Nb1) and cultures were expressed for an additional 30 hours before cell harvesting by centrifugation at 5400 relative centrifugal force (rcf).

Cell pellets were resuspended in a lysis/wash buffer [50 mM tris, 500 mM NaCl, and 5 mM imidazole (pH 7.5)] and lysed using an M-110P microfluidizer system (Microfluidics Corp, USA) set at 18,000 psi. Cell debris was pelleted at 20,900 rcf for 25 min at 4°C and clarified cell lysate was recovered. To bind His $_6$ -tagged protein, clarified cell lysate was incubated with 500 μ l of TALON cobalt NTA resin (Takara Bio, Japan) at 4°C for 1 hour with rocking. Resin was collected and extensively washed with 50 resin bed volumes (bv) of lysis buffer.

For proteins containing an N-terminal His-bdSUMO tag, the resin was resuspended in 3 bvs of storage buffer (50 mM tris,

500 mM NaCl, and 10% glycerol). Untagged bdSENP1 [100 nM, (36, 37)] was added to the resuspension, and the solution was incubated for 1 hour at room temperature with rocking. The resin was retained in a column and cleaved Nb was collected in the flow through. For all other constructs, bound protein was eluted from the TALON resin by incubation with 5 by of elution buffer (lysis buffer with 200 mM imidazole) and desalted into storage buffer using a PD-10 delating column according to the manufacturer's instructions. If cleavage of a TEV-GFP-HIS tag was required, TEV protease was added to the desalted solution and incubated overnight at 4°C. Following incubation, cleaved protein was rerun over TALON resin to bind the cleaved tag, and the flow through containing the Nb was collected. When necessary, the protein solution was concentrated by using a 3-kDa MWCO Vivaspin spin-concentration filter (GE Health Sciences). Protein concentration was determined by absorbance at 280 nm and flash-frozen with liquid nitrogen and stored at -80°C until needed.

Mobility shift assay

To quantify the reactivity of purified Tet3.0-Nbs, SDS-PAGE mobility shift assays were used. Tet3.0-incorporated Nbs (~4 μ M) were reacted with approximately 10 M equivalents of sTCO-PEG5k polymer for 10 min on ice. SDS sample buffer (4×) [250 mM tris, 10% (w/v) sodium dodecyl sulfate, 50% (v/v) glycerol, 20% (v/v) β -mercaptoethanol, and 0.1% (w/v) bromophenol blue (pH 6.8)] was added before incubation at 95°C for approximately 5 min. Samples were then loaded onto 15 or 17% SDS-PAGE gels and run at 200 V for approximately 60 min, followed by Coomassie stain solution.

Tet3.0-sTCO conjugation reactions

To Tet3.0-containing Nbs (150 to 200 $\mu M)$, sTCO-functionalized PEG linkers (solubilized in dimethyl sulfoxide to a final concentration of 10 mM or 1 mM) were slowly mixed in reaction buffer [50 mM tris, 500 mM NaCl, and 10% glycerol (pH 7.5)] for a total reaction volume of 500 μl . The ratio of sTCO-PEG linker to Tet3.0-Nb was experimentally determined (fig. S6). The reaction proceeded for 10 to 30 min at room temperature, after which the resulting products were centrifuged at 21,000 rcf for 15 min to remove any precipitation products before gel filtration.

Size exclusion chromatography

To purify Nb complexes, homodimeric conjugation products were gel-filtered with a size exclusion column Superdex 200 10/300 (GE Healthcare) and heterodimeric and trimeric conjugation products were gel-filtered with a Superdex 75 16/600 size exclusion column (GE Healthcare). The columns were equilibrated in 2 column volumes of reaction buffer, and 500 μ l of clarified reaction material was injected onto the columns. The elution of the desired material was monitored by tracking the A_{280} , and eluted fractions were analyzed with SDS-PAGE (see the Supplementary Materials). The purified proteins were collected, concentrated, frozen in liquid nitrogen, and stored at -80° C for subsequent experimentation.

Mass spectrometry

Nb samples were desalted into liquid chromatography–MS grade water with NAP-5 columns according to the manufacturer's instructions. The Nb samples were diluted to $10~\mu M$ in 15% acetonitrile and 0.1% formic acid before analysis using an Agilent 6545XT quadrupole

time-of-flight mass spectrometer. The instrument was modified with an ExD cell (e-MSion Inc.) to enable electron capture dissociation. A custom nanoelectrospray source was used to ionize the samples. Briefly, 5 µl of sample was loaded into the back of a 10-cm borosilicate glass capillary (Sutter Instrument Co.) with an OD of 1 mm and an inside diameter of 0.78 mm. The tip was loaded into the capillary holder with a platinum wire placed into the solution. The capillary holder with the emitter was positioned in front of the instrument inlet and ionized with a potential of 1200 V. The instrument was operating in the 2-GHz high-resolution mode during analysis. The mass range for MS1 and MS2 spectra was 120 to 3200 m/z (mass/ charge ratio). Intact masses were determined using the Agilent MassHunter BioConfirm Deconvolution algorithm, and the fragmentation data were analyzed with the ExD Viewer (Version 4.1.13). Peptide fragment ions were identified by considering the similarity of the theoretical m/z and the isotopic cluster intensities. The resulting matches were manually curated to ensure quality of assignments.

Biolayer interferometry

BLI measurements were made on a FortéBIO (Menlo Park, CA) Octet Red96 system using anti-human capture (AHC) sensors, which are immobilized with anti-human Fc antibodies. Assays were performed in 96-well microplates at 30°C. All sample volumes were 200 µl. AHC tips were conditioned by three rounds of incubation in 10 mM glycine (pH 1.7) for 5 s followed by incubation in running buffer [10 mM Hepes (pH 7.6), 150 mM NaCl, 3 mM EDTA, 0.005% Tween 20, and 1 bovine serum albumin (mg/ml)] for 5 s. Conditioning was followed by baseline establishment in running buffer for 150 s and loading with SARS-CoV-2 RBD tagged with a C-terminal Fc tag (ACRO Biosystems, 0.005 µg/Ulf) for 95 s. After loading SARS-CoV-2-RBD-Fc onto AHC sensors, a second baseline was established in running buffer (150 s) and association with VHH12 Nb variants (2 to 1500 nM for global fits; see table S2) was carried out in the same buffer for 200 s. Dissociation was subsequently measured in the same buffer for 700 s.

Statistical analysis of BLI fits

Data were reference-subtracted and aligned with each other in the Octet Data Analysis software (FortéBIO). Sensorgrams were fit with a 1:2 (bivalent analyte) binding model to obtain kinetic binding constants for homodimers, and a 1:1 binding model to obtain kinetic binding constants for heterodimer and trimer. Equilibrium $K_{\rm d}$ values were calculated from the ratio of $k_{\rm off}$ to $k_{\rm on}$. Global fits with an R^2 higher than 0.98 were considered acceptable.

Pseudovirus neutralization assay

The pseudovirus neutralization assay was performed as described previously (31) with the following changes. 293T-hACE2 (human angiotensin-converting enzyme 2) cells were seeded into white 96-well plates at 1×10^4 cells per well and grown for 24 hours. Nbs were serially diluted into storage buffer [30 mM tris (pH 7.5), 500 mM NaCl, and 10% glycerol] to $10\times$ the test concentration. Pseudovirus was added to each to dilution to make $1\times$ test concentration. These were incubated at 37° C for 1 hour. Polybrene was added as previously described (31). Media were removed from the 96-well plates and replaced with the pseudovirus-Nb mixture or pseudovirus-buffer alone mixture at $150~\mu$ l per well in triplicate. After 48 hours, cell viability and luciferase activity were assessed with the ONE-Glo + Tox luciferase reporter and cell viability assay kit (Promega).

Infectivity was defined as the luciferase signal from infected 293T-hACE2 cells. One-way analysis of variance (ANOVA) was performed between experimental and control samples. P value was calculated by unpaired two-tailed Student's t test. P < 0.05 was considered statistically significant.

SUPPLEMENTARY MATERIALS

Supplementary material for this article is available at https://science.org/doi/10.1126/sciadv.abm6909

View/request a protocol for this paper from Bio-protocol.

REFERENCES AND NOTES

- 1. S. Muyldermans, Applications of nanobodies. Annu. Rev. Anim Biosci. 9, 401-421 (2021).
- S. Muyldermans, A guide to: Generation and design of nanobodies. FEBS J. 288, 2084–2102 (2021).
- P. Bannas, J. Hambach, F. Koch-Nolte, Nanobodies and nanobody-based human heavy chain antibodies as antitumor therapeutics. Front. Immunol. 8, 45–57 (2017).
- P.-A. Koenig, H. Das, H. Liu, B. M. Kümmerer, F. N. Gohr, L.-M. Jenster, L. D. J. Schiffelers, Y. M. Tesfamariam, M. Uchima, J. D. Wuerth, K. Gatterdam, N. Ruetalo, M. H. Christensen, C. I. Fandrey, S. Normann, J. M. P. Tödtmann, S. Pritzl, L. Hanke, J. Boos, M. Yuan, X. Zhu, J. L. Schmid-Burgk, H. Kato, M. Schindler, I. A. Wilson, M. Geyer, K. U. Ludwig, B. M. Hällberg, N. C. Wu, F. I. Schmidt, Structure-guided multivalent nanobodies block SARS-CoV-2 infection and suppress mutational escape. Science 371, eabe6230 (2021).
- S. Bessalah, S. Jebahi, N. Mejri, I. Salhi, T. Khorchani, M. Hammadi, Perspective on therapeutic and diagnostic potential of camel nanobodies for coronavirus disease-19 (COVID-19). Biotech 11, 89–90 (2021).
- J. Huo, H. Mikolajek, A. Ie Bas, J. J. Clark, P. Sharma, A. Kipar, J. Dormon, C. Norman, M. Weckener, D. K. Clare, P. J. Harrison, J. A. Tree, K. R. Buttigieg, F. J. Salguero, R. Watson, D. Knott, O. Carnell, D. Ngabo, M. J. Elmore, S. Fotheringham, A. Harding, L. Moynié, P. N. Ward, M. Dumoux, T. Prince, Y. Hall, J. A. Hiscox, A. Owen, W. James, M. W. Carroll, J. P. Stewart, J. H. Naismith, R. J. Owens, A potent SARS-CoV-2 neutralising nanobody shows therapeutic efficacy in the Syrian golden hamster model of COVID-19. *Nat. Commun.* 12, 5469 (2021).
- L. S. Mitchell, L. J. Colwell, Comparative analysis of nanobody sequence and structure data. Proteins 86, 697–706 (2018).
- D. Schumacher, J. Helma, A. F. L. Schneider, H. Leonhardt, C. P. R. Hackenberger, Nanobodies: Chemical functionalization strategies and intracellular applications. *Angew. Chem. Int. Ed. Engl.* 57, 2314–2333 (2018).
- K. Els Conrath, M. Lauwereys, L. Wyns, S. Muyldermans, Camel single-domain antibodies as modular building units in bispecific and bivalent antibody constructs. J. Biol. Chem. 276, 7346–7350 (2001).
- S. L. Harwood, A. Alvarez-Cienfuegos, N. Nuñez-Prado, M. Compte, S. Hernández-Pérez, N. Merino, J. Bonet, R. Navarro, P. M. P. Van Bergen En Henegouwen, S. Lykkemark, K. Mikkelsen, K. Mølgaard, F. Jabs, L. Sanz, F. J. Blanco, P. Roda-Navarro, L. Alvarez-Vallina, ATTACK, a novel bispecific T cell-recruiting antibody with trivalent EGFR binding and monovalent CD3 binding for cancer immunotherapy. *Oncoimmunology* 7, e1377874 (2017).
- M. Compte, S. L. Harwood, I. G. Muñoz, R. Navarro, M. Zonca, G. Perez-Chacon,
 A. Erce-Llamazares, N. Merino, A. Tapia-Galisteo, A. M. Cuesta, K. Mikkelsen, E. Caleiras,
 N. Nuñez-Prado, M. A. Aznar, S. Lykkemark, J. Martínez-Torrecuadrada, I. Melero,
 F. J. Blanco, J. B. de la Serna, J. M. Zapata, L. Sanz, L. Alvarez-Vallina, A tumor-targeted
 trimeric 4-1BB-agonistic antibody induces potent anti-tumor immunity without systemic
 toxicity. Nat. Commun. 9, 4809 (2018).
- J. Zhang, J. Tanha, T. Hirama, N. H. Khieu, R. To, H. Tong-Sevinc, E. Stone, J. R. Brisson, C. R. MacKenzie, Pentamerization of single-domain antibodies from phage libraries: A novel strategy for the rapid generation of high-avidity antibody reagents. *J. Mol. Biol.* 335, 49–56 (2004).
- Y. Huang, T. Liu, Therapeutic applications of genetic code expansion. Synth Syst Biotechnol 3. 150–158 (2018).
- C. H. Kim, J. Y. Axup, A. Dubrovska, S. A. Kazane, B. A. Hutchins, E. D. Wold, V. V. Smider, P. G. Schultz, Synthesis of bispecific antibodies using genetically encoded unnatural amino acids. J. Am. Chem. Soc. 134, 9918–9921 (2012).
- J. Y. Axup, K. M. Bajjuri, M. Ritland, B. M. Hutchins, C. H. Kim, S. A. Kazane, R. Halder, J. S. Forsyth, A. F. Santidrian, K. Stafin, Y. Lu, H. Tran, A. J. Seller, S. L. Biroc, A. Szydlik, J. K. Pinkstaff, F. Tian, S. C. Sinha, B. Felding-Habermann, V. V. Smider, P. G. Schultz, Synthesis of site-specific antibody-drug conjugates using unnatural amino acids. *Proc. Natl. Acad. Sci. U.S.A.* 109, 16101–16106 (2012).
- R. Fu, L. Carroll, G. Yahioglu, E. O. Aboagye, P. W. Miller, Antibody fragment and affibody ImmunoPET imaging agents: Radiolabelling strategies and applications. *ChemMedChem* 13, 2466–2478 (2018).

SCIENCE ADVANCES | RESEARCH ARTICLE

- A. Yamaguchi, T. Matsuda, K. Ohtake, T. Yanagisawa, S. Yokoyama, Y. Fujiwara,
 T. Watanabe, T. Hohsaka, K. Sakamoto, Incorporation of a doubly functionalized synthetic amino acid into proteins for creating chemical and light-induced conjugates.

 Bioconjug. Chem. 27, 198–206 (2016).
- S. A. Costa, D. Mozhdehi, M. J. Dzuricky, F. J. Isaacs, E. M. Brustad, A. Chilkoti, Active targeting of cancer cells by nanobody decorated polypeptide micelle with bio-orthogonally conjugated drug. *Nano Lett.* 19, 247–254 (2019).
- K. W. Yong, D. Yuen, M. Z. Chen, C. J. H. Porter, A. P. R. Johnston, Pointing in the right direction: Controlling the orientation of proteins on nanoparticles improves targeting efficiency. *Nano Lett.* 19, 1827–1831 (2019).
- R. W. Cheloha, T. J. Harmand, C. Wijne, T. U. Schwartz, H. L. Ploegh, Exploring cellular biochemistry with nanobodies. J. Biol. Chem. 295, 15307–15327 (2020).
- H. S. Jang, S. Jana, R. J. Blizzard, J. C. Meeuwsen, R. A. Mehl, Access to faster eukaryotic cell labeling with encoded tetrazine amino acids. J. Am. Chem. Soc. 142, 7245–7249 (2020).
- R. J. Blizzard, T. E. Gibson, R. A. Mehl, Site-specific protein labeling with tetrazine amino acids. Methods Mol. Biol. 1728, 201–217 (2018).
- A. F. Chaparro Sosa, R. M. Bednar, R. A. Mehl, D. K. Schwartz, J. L. Kaar, Faster surface ligation reactions improve immobilized enzyme structure and activity. *J. Am. Chem. Soc.* 143, 7154–7163 (2021).
- R. M. Bednar, T. W. Golbek, K. M. Kean, W. J. Brown, S. Jana, J. E. Baio, P. A. Karplus, R. A. Mehl, Immobilization of proteins with controlled load and orientation. ACS Appl Mater Interfaces 11, 36391–36398 (2019).
- F. Chen, Z. Liu, F. Jiang, Prospects of neutralizing nanobodies against SARS-CoV-2. Front. Immunol. 12, 690742 (2021).
- D. Wrapp, D. De Vlieger, K. S. Corbett, G. M. Torres, N. Wang, W. Van Breedam, K. Roose, L. van Schie; VIB-CMB COVID- Response Team, M. Hoffmann, S. Pöhlmann, B. S. Graham, N. Callewaert, B. Schepens, X. Saelens, J. S. M. Lellan, Structural basis for potent neutralization of betacoronaviruses by single-domain camelid antibodies. *Cell* 181, 1004–1015.e5 (2020).
- K. W. Yong, D. Yuen, M. Z. Chen, A. P. R. Johnston, Engineering the orientation, density, and flexibility of single-domain antibodies on nanoparticles to improve cell targeting. ACS Appl. Mater. Interfaces 12, 5593–5600 (2020).
- J. Huo, A. L. Bas, R. R. Ruza, H. M. E. Duyvesteyn, H. Mikolajek, T. Malinauskas, T. K. Tan, P. Rijal, M. Dumoux, P. N. Ward, J. Ren, D. Zhou, P. J. Harrison, M. Weckener, D. K. Clare, V. K. Vogirala, J. Radecke, L. Moynié, Y. Zhao, J. Gilbert-Jaramillo, M. L. Knight, J. A. Tree, K. R. Buttigieg, N. Coombes, M. J. Elmore, M. W. Carroll, L. Carrique, P. N. M. Shah, W. James, A. R. Townsend, D. I. Stuart, R. J. Owens, J. H. Naismith, Neutralizing nanobodies bind SARS-CoV-2 spike RBD and block interaction with ACE2. Nat. Struct. Mol. Biol. 27, 846–854 (2020).
- E. M. Obeng, C. K. O. Dzuvor, M. K. Danquah, Anti-SARS-CoV-1 and -2 nanobody engineering towards avidity-inspired therapeutics. *Nano Today* 42, 101350 (2022).
- K. H. D. Crawford, R. Eguia, A. S. Dingens, A. N. Loes, K. D. Malone, C. R. Wolf, H. Y. Chu, M. A. Tortorici, D. Veesler, M. Murphy, D. Pettie, N. P. King, A. B. Balazs, J. D. Bloom, Protocol and reagents for pseudotyping lentiviral particles with SARS-CoV-2 spike protein for neutralization assays. *Viruses* 12, 513 (2020).

- J. Kim, A. Mukherjee, D. Nelson, A. Jozic, G. Sahay, Rapid generation of circulating and mucosal decoy ACE2 using mRNA nanotherapeutics for the potential treatment of SARS-CoV-2. bioRxiv 10.1101/2020.07.24.205583 (2020).
- 32. L. Presta, Antibody engineering for therapeutics. Curr. Opin. Struct. Biol. 13, 519-525 (2003).
- T. Chanier, P. Chames, Nanobody engineering: Toward next generation immunotherapies and immunoimaging of cancer. Antibodies 8, 13 (2019).
- 34. A. C. Hunt, J. B. Case, Y.-J. Park, L. Cao, K. Wu, A. C. Walls, Z. Liu, J. E. Bowen, H.-W. Yeh, S. Saini, L. Helms, Y. T. Zhao, T.-Y. Hsiang, T. N. Starr, I. Goreshnik, L. Kozodoy, L. Carter, R. Ravichandran, L. B. Green, W. L. Matochko, C. A. Thomson, B. Vögeli, A. Krüger-Gericke, L. A. Van Blargan, R. E. Chen, B. Ying, A. L. Bailey, N. M. Kafai, S. Boyken, A. Ljubetič, N. Edman, G. Ueda, C. Chow, A. Addetia, N. Panpradist, M. Gale Jr., B. S. Freedman, B. R. Lutz, J. D. Bloom, H. Ruohola-Baker, S. P. J. Whelan, L. Stewart, M. S. Diamond, D. Veesler, M. C. Jewett, D. Baker, Multivalent designed proteins protect against SARS-CoV-2 variants of concern. bioRxiv 10.1101/2021.07.07.451375 (2021).
- D. De Vlieger, M. Ballegeer, I. Rossey, B. Schepens, X. Saelens, Single-domain antibodies and their formatting to combat viral infections. *Antibodies* 8, 1 (2018).
- S. Frey, D. Gorlich, A new set of highly efficient, tag-cleaving proteases for purifying recombinant proteins. J. Chromatogr. A 1337, 95–105 (2014).
- S. Frey, D. Gorlich, Purification of protein complexes of defined subunit stoichiometry using a set of orthogonal, tag-cleaving proteases. J. Chromatogr. A 1337, 106–115 (2014).
- E. F. Pettersen, T. D. Goddard, C. C. Huang, G. S. Couch, D. M. Greenblatt, E. C. Meng, T. E. Ferrin, UCSF Chimera—A visualization system for exploratory research and analysis. J. Comput. Chem. 25, 1605–1612 (2004).

Acknowledgments: We are grateful to R. B. Cooley for scientific guidance and discussions. Molecular graphics and analyses performed with UCSF Chimera were developed by the Resource for Biocomputing, Visualization, and Informatics at the University of California, San Francisco, with support from NIH P41-GM103311. Neutralization assays were performed by D. Nelson at the High Throughput Screening Services Lab (HTSSL) at Oregon State University. Funding: This work was supported in part by National Science Foundation grants NSF-1518265 and NSF-2054824 and National Institute of General Medical Sciences grants R01GM131168 and RM1-GM144227 to R.A.M. and Oregon State University SciRIS-2 funding. 2019-2021, chemically functionalized nanobodies to R.A.M. Author contributions: Conceptualization: E.M.V.F., R.M.B., S.J., and R.A.M. Methodology: E.M.V.F., R.M.B., S.J., R.F., and J.B. Investigation: E.M.V.F., R.M.B., S.J., and R.F. Supervision: R.A.M. and J.B. Writing—original draft: E.M.V.F. Writing—review and editing: E.M.V.F., P.A.K., and R.A.M. Competing interests: R.A.M., E.M.V.F, and R.M.B. are inventors on a patent related to this work filed by Oregon State University (no. 63/285,315, filed 2 December 2021). All other authors declare that they have no competing interests. Data and materials availability: All data needed to evaluate the conclusions in the paper are present in the paper and/or the Supplementary Materials. The GCE plasmids can be provided by Addgene pending scientific review and a completed material transfer agreement.

Submitted 5 October 2021 Accepted 23 March 2022 Published 6 May 2022 10.1126/sciadv.abm6909

Science Advances

Nanobody assemblies with fully flexible topology enabled by genetically encoded tetrazine amino acids

Elise M. Van FossenRiley M. BednarSubhashis JanaRachel FranklinJoseph BeckmanP. Andrew KarplusRyan A. Mehl

Sci. Adv., 8 (18), eabm6909. • DOI: 10.1126/sciadv.abm6909

View the article online

https://www.science.org/doi/10.1126/sciadv.abm6909 **Permissions**

https://www.science.org/help/reprints-and-permissions